

# Cosmic Web Reconstruction through Density Ridges: Catalogue

Yen-Chi Chen,<sup>1,3\*</sup> Shirley Ho,<sup>2,3</sup> Jon Brinkmann,<sup>4</sup> Peter E. Freeman,<sup>1,3</sup>  
Christopher R. Genovese,<sup>1,3</sup> Donald P. Schneider,<sup>5,6</sup> Larry Wasserman<sup>1,3</sup>

<sup>1</sup>*Department of Statistics, Carnegie Mellon University, Pittsburgh, PA 15213, USA*

<sup>2</sup>*Department of Physics, Carnegie Mellon University, Pittsburgh, PA 15213, USA*

<sup>3</sup>*McWilliams Center for Cosmology, Carnegie Mellon University, Pittsburgh, PA 15213, USA*

<sup>4</sup>*Apache Point Observatory, Sunspot, NM 88349, USA*

<sup>5</sup>*Department of Astronomy and Astrophysics, The Pennsylvania State University, University Park, PA 16802, USA*

<sup>6</sup>*Institute for Gravitation and the Cosmos, The Pennsylvania State University, University Park, PA 16802, USA*

23 September 2015

## ABSTRACT

We construct a catalogue for filaments using a novel approach called SCMS (subspace constrained mean shift; Ozertem & Erdogmus 2011; Chen et al. 2015). SCMS is a gradient-based method that detects filaments through density ridges (smooth curves tracing high-density regions). A great advantage of SCMS is its uncertainty measure, which allows an evaluation of the errors for the detected filaments. To detect filaments, we use data from the Sloan Digital Sky Survey, which consist of three galaxy samples: the NYU main galaxy sample (MGS), the LOWZ sample and the CMASS sample. Each of the three dataset covers different redshift regions so that the combined sample allows detection of filaments up to  $z = 0.7$ .

Our filament catalogue consists of a sequence of two-dimensional filament maps at different redshifts that provide several useful statistics on the evolution cosmic web. To construct the maps, we select spectroscopically confirmed galaxies within  $0.050 < z < 0.700$  and partition them into 130 bins. For each bin, we ignore the redshift, treating the galaxy observations as a 2-D data and detect filaments using SCMS. The filament catalogue consists of 130 individual 2-D filament maps, and each map comprises points on the detected filaments that describe the filamentary structures at a particular redshift.

We also apply our filament catalogue to investigate galaxy luminosity and its relation with distance to filament. Using a volume-limited sample, we find strong evidence ( $6.1\sigma - 12.3\sigma$ ) that galaxies close to filaments are generally brighter than those at significant distance from filaments.

**Key words:** (cosmology:) large-scale structure of Universe – catalogues

## 1 INTRODUCTION

Matter in the Universe tends to be distributed in a network-like large-scale structure which is known as the cosmic web (Bond et al. 1996). The existence of this filamentary structure has been confirmed observationally and can be reproduced in N-body simulations (Jenkins et al. 1998; Colberg et al. 2005; Springel et al. 2005; Dolag et al. 2006). The large-scale structure comprises four distinct objects: overdense clusters, interconnected filaments, widespread sheet-like walls and large empty voids. In this paper, we focus on cosmic filaments.

The principal approach to study large-scale structure is by constructing a catalogue. For galaxy clusters, several catalogues have been created; see, e.g., Abell catalogue (Abell et al. 1989), redMaPPer (Rykoff et al. 2014; Rozo & Rykoff 2014), XCS (Menanteau et al. 2013), MCMC (Piffaretti et al. 2011), Mantz (Mantz et al. 2010), and Planck ESZ (Planck Collaboration et al. 2011). However, there exists few catalogues for filaments (a recent example can be found in Tempel et al. 2014). There are three reasons why high-quality filament catalogues are needed.

First, catalogues for filaments provide a reference to other types of large-scale structures. It is known that galaxy clusters are connected by filaments; filaments are mainly distributed on cosmic sheets/walls and surround large empty

\* E-mail: yenchic@andrew.cmu.edu

voids. With a catalogue of filaments, it is easier to identify other large-scale structures.

Second, filamentary structure at different redshifts can be used to probe cosmological models. In N-body simulations, we observe how a small fluctuation in the initial density field, magnified by gravitational force over time, weaves matter into a web-like structure (Jenkins et al. 1998; Colberg et al. 2005; Springel et al. 2005; Dolag et al. 2006). The evolution of the cosmic web depends on the initial condition of the early Universe. Thus, how filaments change as a function of redshift conveys information about dark matter and dark energy.

Finally, filament catalogues make it easier to study properties of filaments and their interaction with nearby galaxies. For example, recent simulations have shown that galaxy intrinsic alignments and luminosity are impacted by nearby filaments (Codis et al. 2015). Orientations of filaments are also found to be correlated with the shape, angular momentum and peculiar velocity of dark matter haloes (Hahn et al. 2007b,a, 2009; Paz et al. 2008; Zhang et al. 2009, 2013; Forero-Romero et al. 2014). Despite the abundance of results on simulation studies, few measurements regarding galaxies aligned along filaments have been obtained (see Jones et al. (2010) and Guo et al. (2015) for some results in spin alignment and luminosity).

In this paper, we present a catalogue for filaments using a novel approach called SCMS (subspace constrained mean shift, Ozertem & Erdogmus 2011) that models filaments as ridges of the galaxy probability density function. SCMS first estimates galaxy density fields, then uses a gradient ascent method to detect ridges; ridges are curve-like, smooth structures that characterize high-density regions. SCMS has two appealing properties. First, SCMS consistently detects filaments in the sense that the intersections between filaments generally are populated by galaxy clusters (See Section 5.2 and Chen et al. 2015), as confirmed by other galaxy cluster detections (Rykoff et al. 2014; Rozo & Rykoff 2014). Second, SCMS is equipped with a statistically consistent measure of uncertainty (Chen et al. 2014a) that allows an evaluation of the error for filament detection.

To construct the filament maps, we use a combined galaxy sample from Sloan Digital Sky Survey (SDSS; York et al. 2000; Eisenstein et al. 2011) that consists of the three datasets: NYU MGS, LOWZ and CMASS samples. We focus on redshifts between  $z = 0.050 - 0.700$  since the observed number density within this region is sufficiently high to generate statistically meaningful results. We first partition the Universe according to redshift into thin slices of width  $\Delta z = 0.005$ , then perform SCMS within each slice. The above process yields a series of filament maps that characterize the filamentary structure of the Universe at different redshifts. The variation of filament maps at different redshifts provides information about the evolution of the Universe that can be further used to constrain cosmology. We can construct filament maps for future photometric surveys (e.g. LSST) or spectroscopic surveys (e.g. WFIRST and Euclid) by applying SCMS to these data.

To demonstrate the usefulness of our filament maps, we investigate the relationship between the luminosity of a galaxy and its distance to nearby filaments. We separate the three samples (NYU MGS, LOWZ and CMASS) and compare galaxy luminosity versus its distance to filaments.

There is strong evidence that galaxies near filaments tend to be brighter than those away from filaments.

In this paper, we assume a WMAP 7  $\Lambda$ CDM cosmology with  $H_0 = 70$ ,  $\Omega_m = 0.274$ , and  $\Omega_\Lambda = 0.726$  (Anderson et al. 2012, 2014).

## 2 MODELS AND METHODS

### 2.1 SCMS: Detecting Filaments through Density Ridges

We adopt the Subspace Constrain Mean Shift (SCMS; Ozertem & Erdogmus 2011) algorithm to construct filament maps for slices of our Universe at various redshifts. We use the version of SCMS described in Chen et al. (2015). SCMS detects filaments as galaxy density ridges (Chen et al. 2014a) and uses a three-step algorithm (density estimation, thresholding and gradient ascent) to detect filaments. Detailed implementations of SCMS can be found in Ozertem & Erdogmus (2011) and Chen et al. (2015). Here we briefly discuss how density ridges are detected by SCMS.

Let  $X_1, \dots, X_n$  denote the locations of galaxies and

$$p(x) = \frac{1}{nh^3} \sum_{i=1}^n K\left(\frac{\|x - X_i\|}{h}\right), \quad (1)$$

be the kernel density estimator where  $h$  is the smoothing bandwidth that controls the degree of smoothing,  $K$  is the Gaussian kernel, and  $\|x - y\|$  is the Euclidean distance between  $x$  and  $y$ . Note that  $p$  is also known as the kernel density estimator (KDE) in statistical literature (Wasserman 2006). We further define  $g(x) = \nabla p(x)$  and  $H(x) = \nabla \nabla p(x)$  to be the gradient and the Hessian matrix of  $p(x)$ , respectively.

The *density ridges* (Eberly 1996; Ozertem & Erdogmus 2011; Genovese et al. 2014; Chen et al. 2014b,a) of  $p$  are the collection of points

$$R = \{x : v_j^T(x)g(x) = 0, j = 2, 3, \lambda_2(x) < 0\}, \quad (2)$$

where  $v_j(x)$ ,  $\lambda_j(x)$  are the  $j$ -th eigenvector and eigenvalue, respectively, of  $H(x)$  and  $p_0$  is a density threshold. Essentially, SCMS outputs a set of points on  $R$ . See Figure 1 for an example.

The idea of using eigen-structures of Hessian matrix of the galaxy density to detect filaments has been used in other filament finders; see, e.g., the skeleton (Novikov et al. 2006), the Multiscale Morphology Filter (MMF; Arag3n-Calvo et al. 2007, 2010a), the Smoothed Hessian Major Axis Filament Finder (SHMAFF; Bond et al. 2010b,a), the Spine method (Arag3n-Calvo et al. 2010b), and the DisPerSE model (Sousbie 2011).

### 2.2 SCMS: Uncertainty Measure

An appealing property of SCMS is its uncertainty measure. We measure the error for filament detection via the bootstrap technique (Efron 1979). We bootstrap the original data and apply SCMS to the bootstrap sample. This exercise provides gives a set of bootstrap filaments. We then compute the (projection) distances from  $R$  (a filament detected in the original sample) to each bootstrap filament. Thus, each point on  $R$  will be assigned an error value. By repeating the

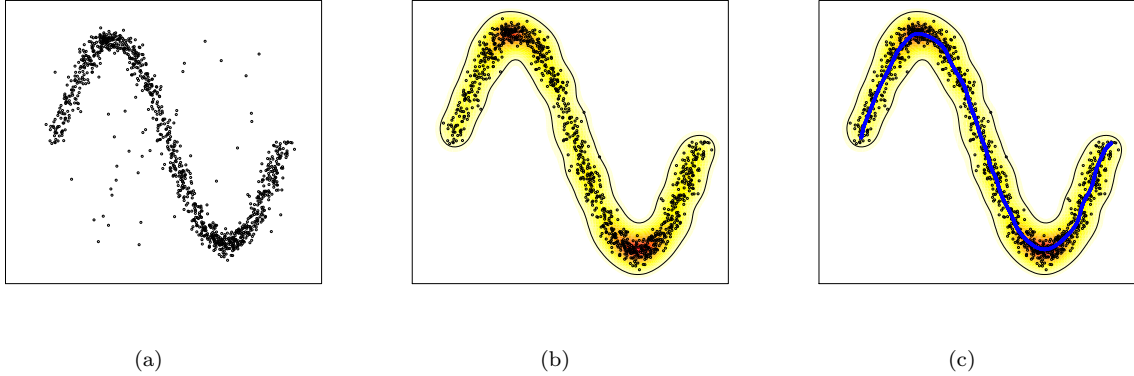


**Figure 1.** An illustration of the SCMS technique. **(a):** The original data. **(b):** Kernel density estimation (red-yellow: high density regions) and thresholding (removing points in low density regions). **(c):** The ridge estimation (blue curve). Essentially, the SCMS technique is to identify ridges in the galaxy density function estimated by the KDE; see section §2.1 for more involved discussion.

bootstrap multiple times, for example 1,000 times, every point on  $R$  has 1,000 error values. The mean of these bootstrap error values for each point is the uncertainty measure to the filaments detected by SCMS. More detailed discussion on the uncertainty measure can be found in [Chen et al. \(2015\)](#).

### 2.3 Slicing the Universe

The observed galaxy locations contain three variables, namely, the right ascension  $\alpha_{2000}$ , the declination  $\delta_{2000}$ , and the redshift  $z$ . We partition the range of redshift into several small intervals; this procedure slices of the Universe. We apply SCMS to galaxies within each slice to detect filaments.

We slice the Universe for three purposes. First, this action removes the Finger-of-God effect since galaxies at the same slice share nearly the same redshift. The Finger-of-God effect is produced by the small peculiar velocities of galaxies, so galaxy clusters are stretched out along the line of sight in redshift space. Thus, most filaments appear to be pointing toward the Earth although they may not really stretch along the line of sight.

Second, slicing the redshift Universe reduces the computational cost dramatically. There are two barriers for computational complexity for SCMS. One is the number of initialized points. In the third step of SCMS (filament detection), we must select many initial grid points to perform an ascending process. This ascending process, called subspace constrained mean shift, pushes points until they arrive at ridges. The size of the Universe greatly increases as the redshift increases, so we need many grid points to detect filaments. The other barrier for the computation is that SCMS requires evaluation of the Hessian of density function, which is known to be computationally intensive if the number of points is large or the dimension is high. Taking slices of the Universe reduces the dimension to two, and for each slice the sample size (the number of galaxies) is small so that SCMS can be performed within reasonable time.

Third, slicing the Universe according to the redshift allows a comparison of filamentary structures at different redshifts. Characteristics of filaments at different redshifts re-

veal information about the nature of our Universe that can be used to constrain cosmological parameters.

## 3 THE SDSS DATA

We use a combined SDSS dataset that contains main galaxy sample (MGS) from DR7 and LOWZ and CMASS samples from DR12 ([Alam et al. 2015](#)). We describe the datasets in detail in the following sections:

### 3.1 The NYU MGS Catalogue

The SDSS DR7 ([Abazajian et al. 2009](#)) contains the completed data set of SDSS-I and SDSS-II. These surveys obtained wide-field CCD photometry ([Gunn et al. 1998, 2006](#)) in five passbands ( $u, g, r, i, z$  [Fukugita et al. 1996; Doi et al. 2010](#)), internally calibrated using the ‘uber-calibration’ process described in [Padmanabhan et al. \(2008\)](#), amassing a total footprint of  $11,663 \text{ deg}^2$ . From this imaging data, galaxies within a footprint of  $9380 \text{ deg}^2$  ([Abazajian et al. 2009](#)) were selected for spectroscopic observation as part of the main galaxy sample ([Strauss et al. 2002](#)), which, to good approximation, consists of all galaxies with  $r_{pet} < 17.77$ , where  $r_{pet}$  is the extinction-corrected r-band Petrosian magnitude. In this analysis we do not consider the Luminous Red Galaxy extension of this program to higher redshift ([Eisenstein et al. 2001](#)).

We obtain the SDSS DR7 Main Galaxy Sample from the NYU value-added catalog (NYU VAGC, [Blanton et al. 2005; Padmanabhan et al. 2008; Adelman-McCarthy et al. 2008](#)). It includes K-corrected absolute magnitudes, and detailed information on the mask. This sample uses galaxies with  $14.5 < r_{pet} < 17.6$ . The  $r_{pet} > 14.5$  limit ensures that only galaxies with reliable SDSS photometry are used and the  $r_{pet} < 17.6$  allows a homogeneous selection over the full footprint of  $6141 \text{ deg}^2$  ([Blanton et al. 2005](#)). Galaxies that did not obtain a redshift due to fibre collisions are assigned the redshift of their nearest neighbour.

### 3.2 The LOWZ and CMASS Catalogues

The LOWZ and CMASS samples are from from Data Release 12 (Alam et al. 2015) of the Sloan Digital Sky Survey SDSS. Together, SDSS I, II, and III imaged over one third of the sky ( $14,555 \text{ deg}^2$ ) in  $u, g, r, i, z$  photometric band-passes to a limiting magnitude of  $r \simeq 22.5$ . The imaging data were processed through a series of pipelines that perform astrometric calibration (Pier et al. 2003), photometric reduction (Lupton et al. 2001), and photometric calibration (Padmanabhan et al. 2008). All of the imaging was reprocessed as part of SDSS Data Release 8 (Aihara et al. 2011).

The Baryon Oscillation Spectroscopic Survey (BOSS) of SDSS-III has obtained spectra and redshifts for 1.35 million galaxies over a footprint covering 10,000 square degrees. These galaxies are selected from the SDSS imaging (Aihara et al. 2011) and were observed together with 160,000 quasars and approximately 100,000 ancillary targets. The targets are assigned to tiles of diameter  $3^\circ$  using an algorithm (Blanton et al. 2003) that adopts to the density of targets on the sky (Blanton et al. 2003). Spectra are obtained using the double-armed BOSS spectrographs (Smee et al. 2013). Each observation is performed in a series of 900-second exposures, integrating until a minimum signal-to-noise ratio is achieved for the faint galaxy targets. This approach ensures a homogeneous data set with a high redshift completeness of more than 97% over the full survey footprint. Redshifts are extracted from the spectra using the methods described in Bolton et al. (2012). A summary of the survey design appears in Eisenstein et al. (2011), a full description of BOSS is provided in Dawson et al. (2013).

BOSS selects two classes of galaxies to be targeted for spectroscopy: ‘LOWZ’ and ‘CMASS’ (we refer the reader to Anderson et al. 2014 for further description of these classes). For the LOWZ sample, the effective redshift is  $z_{\text{eff}} = 0.32$ , slightly lower than that of the SDSS-II luminous red galaxies (LRGs) as we place a redshift cut  $z < 0.43$ . The CMASS selection yields a sample with a median redshift  $z = 0.57$  and a stellar mass that peaks at  $\log_{10}(M/M_\odot) = 11.3$  (Maraston et al. 2013). Most CMASS targets are central galaxies residing in dark matter haloes of mass  $\sim 10^{13} h^{-1} M_\odot$ .

## 4 FILAMENT MAPS

### 4.1 Construction of Filament Maps

We construct filament maps using the three galaxy catalogues: NYU MGS, LOWZ and CMASS. Figure 2 presents some examples of constructed filaments (blue) with galaxies (black) and galaxy clusters (red) from the redMaPPer catalogue. Our construction of filament maps consists of the following steps:

1. Slice the sample between  $0.050 < z < 0.700$  into 130 slices of width  $\Delta z = 0.005$ .
2. Within each slice, select galaxies within  $150^\circ < \alpha_{2000} < 200^\circ$ ,  $5^\circ < \delta_{2000} < 30^\circ$  since this is a relatively complete region for all three galaxy catalogues.
3. Using KDE, compute the mean density and the root mean square (RMS) density for the selected galaxies.

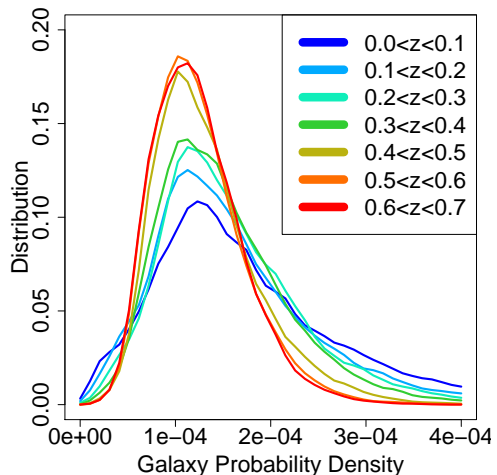


**Figure 3.** Distribution of density profile of filaments at different redshifts. The distribution of density profile is right-skewness at low redshift, indicating that galaxy density on each filament point is in general higher than those filaments at high redshift.

4. Using the root mean square density as a threshold level in SCMS, construct filament maps. The RMS density is used in SCMS as a threshold level to stabilize the algorithm.
5. Apply masks of galaxy catalogues to eliminate filaments outside the region of observations.
6. At each point on filaments, compute the filament’s local direction.

### 4.2 Filament Maps

Our filament map catalogue<sup>1</sup> contains a collection of points on filaments. These points are obtained via SCMS with a uniform grid as the initial points. Thus, one can view the points in the filament maps as a uniformly random sample on all filaments. Each filament point has seven variables as listed in Table 1. The first two ( $\alpha_{2000}, \delta_{2000}$ ) are the location within that slice, and  $z_{\text{low}}$  is the indicator (as well as the lower bound of redshift) for the slice.

The *density* is the galaxy probability density within each slice under the ( $\alpha_{2000}, \delta_{2000}$ )-coordinate at each filament point (the KDE is used to estimate the density). Thus, the total probability within each slice sums to 1. The *density profile*  $\Phi_F \equiv \Phi_F(z)$  is the distribution of density value at each filament point within the same slice and it evolves with redshift. We compare the density profile within different redshift regions in Figure 3. An advantage for using density under ( $\alpha_{2000}, \delta_{2000}$ )-coordinates is that we do not have to renormalize the probability density because the size of each slice remains approximately the same. If we use ordinate cartesian coordinates, the size of each slice increases when the redshift increases. As can be easily seen, at higher redshift, galaxy densities at filament points tends to be lower. The quantity  $H$  is a high-density indicator and is related to the RMS density. If the density of a given filament point is above the RMS density,  $H = 1$ , otherwise it is 0.

<sup>1</sup> The catalogue can be downloaded from <https://sites.google.com/site/yenchicr/catalogue>.

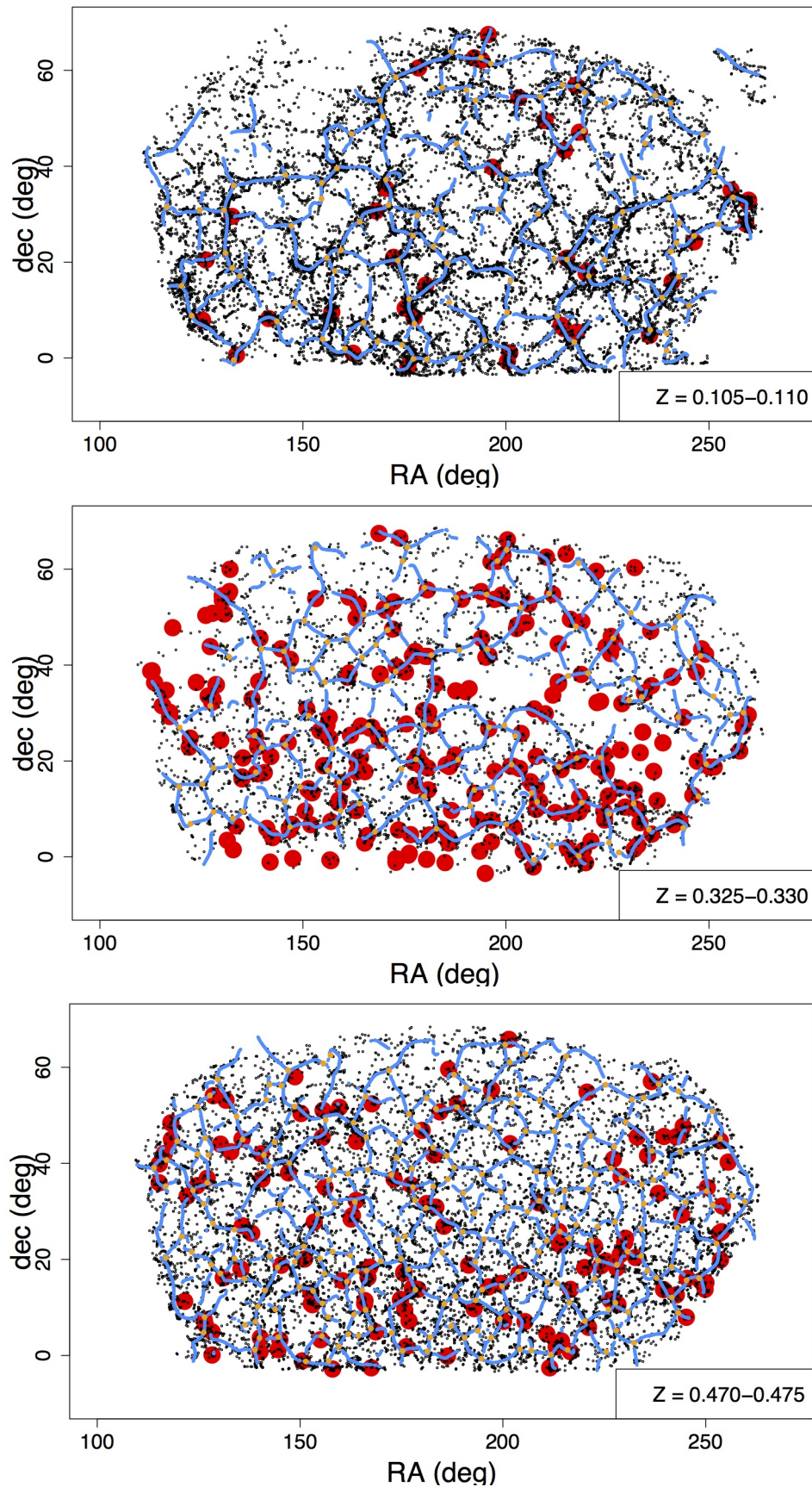


**Figure 2.** Examples for filament maps from the SDSS data. From top to bottom:  $z = 0.105 - 0.110$  (NYU MGS),  $0.325 - 0.330$  (LOWZ) and  $0.470 - 0.475$  (CMASS). The blue curves are detected filaments, the red dots are galaxy clusters from redMaPPer catalogue, and the orange dots are intersections for filaments (details can be found in Appendix 5.2).

Notation	Definition	Comment
$\alpha_{2000}$	Right Ascension	
$\delta_{2000}$	Declination	
$z_{\text{low}}$	Redshift	$z_{\text{low}} \leq z < z_{\text{low}} + 0.005$
density	Galaxy density at each filament point	
H	High density indicator	1: located at high density regions
UM	Uncertainty (Error)	
$v_{\text{ra}}$	Direction of filament	
$v_{\text{dec}}$	Direction of filament	

**Table 1.** Definition of variates in the filament map file.

The quantity UM is the  $1\sigma$  uncertainty (error) for detected filaments. We measure the error for filaments by bootstrapping the SDSS data 100 times. Further details may be found in [Chen et al. \(2014a\)](#).

The last two table’s entries are the orientation of filaments at each filament point. We use the density gradient at each point on filaments as a proxy to the direction. This proxy is known to be stable ([Eberly 1996](#)).

## 5 FILAMENTS AT DIFFERENT REDSHIFTS

The filament maps at each redshift are used to construct a summary file<sup>2</sup> that contains information about filaments at different redshifts. This file consists of a  $130 \times 17$  array. Each row corresponds to a particular slice of the Universe and each column provides information about that slice. We describe all 17 variables in the file in [Table 2](#).

The first variable ( $z_{\text{low}}$ ) is the lower limit on redshift of that slice. Each slice contains the region

$$z_{\text{low}} \leq z < z_{\text{low}} + 0.005.$$

The second variable (N) is the number of galaxies within these regions.  $N_{\text{GC}}$  is the number of galaxy clusters from redMaPPer catalogue ([Rykoff et al. 2014](#); [Roza & Rykoff 2014](#)) within the slice. We use only the clusters with spectroscopic redshifts that are within the mask of each SDSS catalogue. [Figure 5](#) shows N and  $N_{\text{GC}}$  at different redshifts. The left panel displays the galaxy sample size from three samples: the NYU main galaxy sample (black), the LOWZ sample (green) and the CMASS sample (blue). The right panel presents the number of clusters at each slice.

The number h is the smoothing bandwidth used in density reconstruction and filament detection [Chen et al. \(2015\)](#). The left panel of [Figure 6](#) shows the smoothing bandwidth at different redshifts. We select h according to the reference rule in appendix of [Chen et al. \(2015\)](#), which depends on the RMS of the density. h increases as the redshift increases because, at high redshift, the number density of galaxies is small so we need to enforce a strong degree of smoothing to detect filaments. The trend of h is similar to the inverse of the cube root of number density; see the right panel of [Figure 7](#).

The two variables  $\rho_{\text{mean}}, \rho_{\text{rms}}$  are the mean overdensity and the RMS density. The RMS measures the density

fluctuation of  $p(x)$  and is used in the thresholding procedure of the SCMS algorithm ([Chen et al. 2015](#)). We write  $\rho_{\text{mean}}(z) \equiv \bar{\rho}_{\text{mean}}$  and  $\rho_{\text{rms}}(z) \equiv \bar{\rho}_{\text{rms}}$  since the mean density and RMS density change as the redshift changes. The center panel of [Figure 6](#) displays  $\rho_{\text{mean}}(z)$  and  $\rho_{\text{rms}}(z)$ . It is clear that  $\rho_{\text{rms}}(z)$  decreases as redshift increases while the mean density  $\rho_{\text{mean}}(z)$  remains roughly the same. These effects occur for two reasons. First, density fluctuations are smaller at early times (higher redshifts); second, the smoothing parameter h is larger at higher redshifts so that the density estimate is strongly smoothed, reducing the amplitude of fluctuations.

The quantity  $F_{\text{density}}$  is the average density profile of filaments at the given slice and is related to the result in [Figure 3](#), which shows the distribution of density profile at wide-redshift regions. The difference between  $F_{\text{density}}$  and  $\rho_{\text{mean}}$  is that  $F_{\text{density}}$  is the average density value on filaments only while  $\rho_{\text{mean}}$  is the average density value on the whole region of observation. The right panel of [Figure 7](#) presents the over-density for filaments, which is defined as

$$S(z) = \frac{F_{\text{density}}(z) - \rho_{\text{mean}}(z)}{\rho_{\text{rms}}(z)}.$$

The over-density shows how the filaments trace high density regions. If  $S(z)$  is large, then most filaments within this slice trace high density regions. As can be seen, the over-density for filaments decreases as redshift increases, implying that filaments do not trace high density regions so well at the high redshift range. There are many possible explanations for this result. At higher redshift regions, the number density is lower so that our filament reconstruction has larger errors. Another possibility is that, at higher redshift, the smoothing parameter h is also larger, which flattens the density fluctuation.

The quantity  $dF$  is the average distance from all galaxies to filaments within the specified slice. The related quantity  $dF_H$  is analogous to  $dF$ , but uses the distance to ‘high-density’ filaments, i.e., the distance to filament points whose density is above the RMS density. The Left panel of [Figure 7](#) displays  $dF$  at each redshift. The average distance to filaments increases as redshift increases. This increasing pattern is caused by the change in number density– the higher redshift regions generally have lower number density. To demonstrate how number density affects the average distance, we provide the inverse of the cube root of number density at each redshift at right panel of [Figure 7](#); the pattern in the left and right panels are clearly similar.

The quantity  $dF_{\text{gc}}$  is the mean distance to filaments from galaxy clusters (redMaPPer clusters; [Rykoff et al. 2014](#);

<sup>2</sup> See <https://sites.google.com/site/yenchicr/catalogue>.

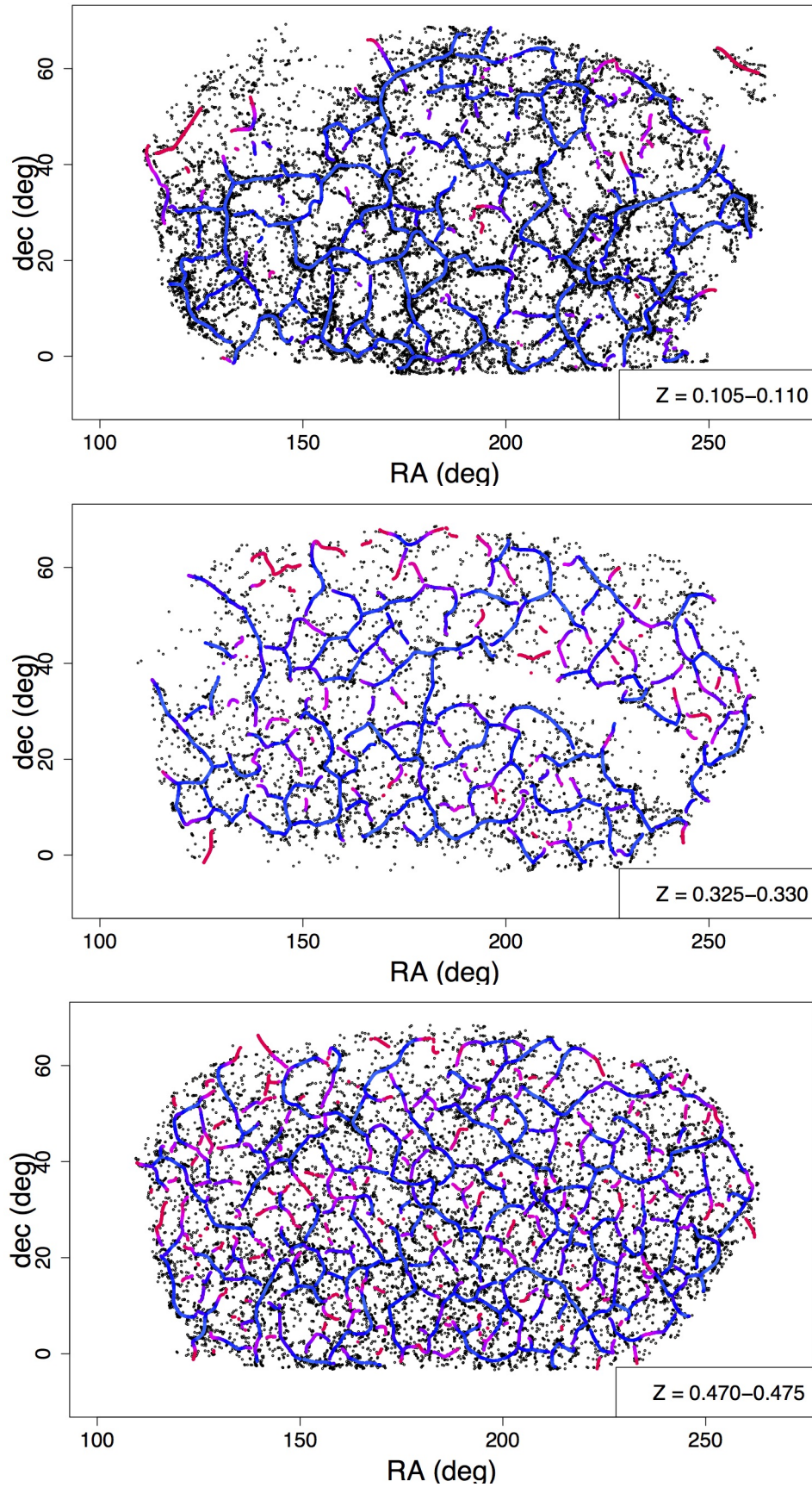


**Figure 4.** Examples of the uncertainty measures of the filament maps. From top to bottom:  $z = 0.105-0.110$  (NYU MGS),  $0.325-0.330$  (LOWZ) and  $0.470-0.475$  (CMASS). We use color to visualize the amount of uncertainty for filament detection (red = high uncertainty). Note that the color is relative uncertainty within each slice.

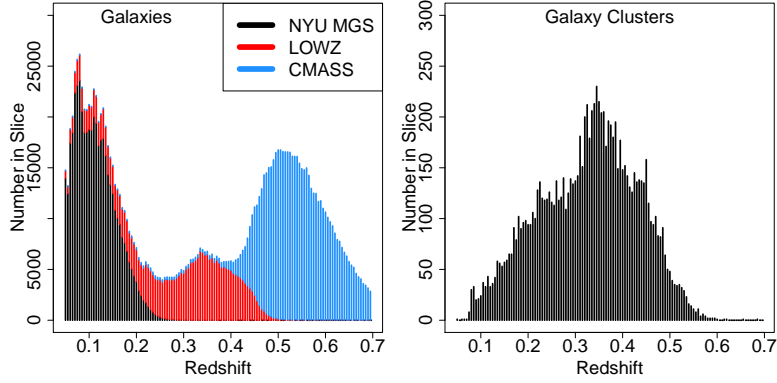


**Figure 5.** **Left:** Number of galaxies within each slice. At boundaries of two catalogues, the number of galaxies per slice is small. **Right:** Number of galaxy clusters from reMaPPer catalogue within each slice. The majority of reMaPPer clusters is in the regions of LOWZ sample.

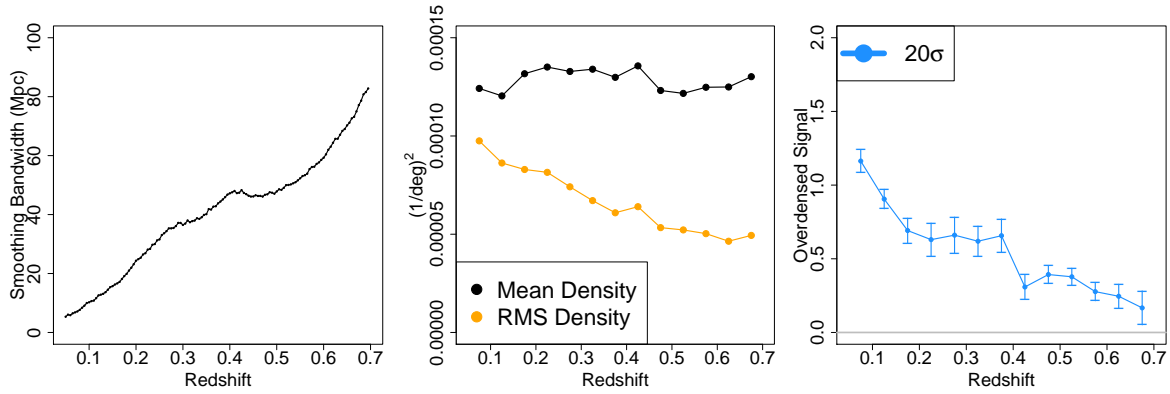


**Figure 6.** **Left:** Smoothing bandwidth over the redshift range 0.05 – 0.70. We must apply a larger smoothing bandwidth for data in higher redshift since the number density decreases. **Center:** The mean and the RMS (probability) density as a function of redshift. In generally, the mean density does not vary too much as the redshift changes. The RMS density, however, decreases when the redshift increases. See §5 for discussion about possibilities for this pattern. **Right:** The overdensified signal at different slices. The overdensified signal is the average density on all filament points within a slice minus  $\rho_{\text{mean}}$  and divide  $\rho_{\text{rms}}$ . The over-density measures the quality of how filament trac high density regions. The decreasing pattern might come from higher errors for detecting filament at higher redshift or the side effect from smoothing. See §5 for more details.

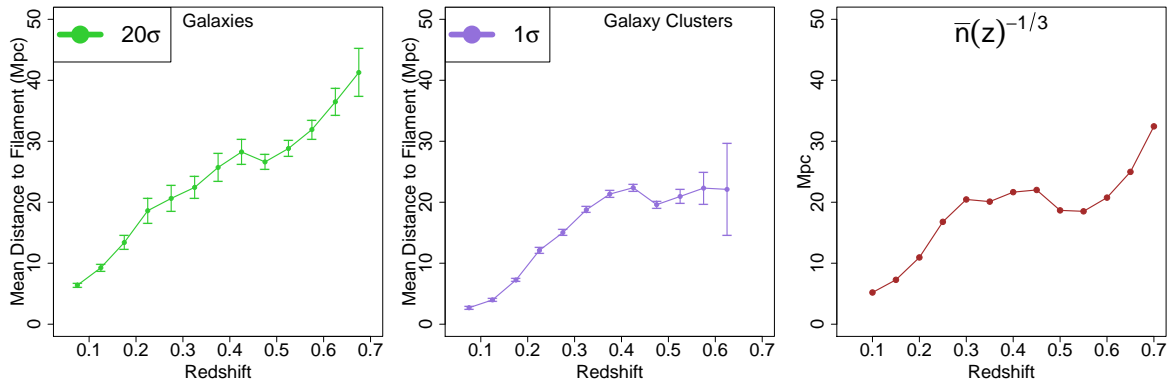


**Figure 7.** **Left :** The distance to filaments from galaxies. The displayed errors for left panel are multiplied by a factor of 20 to show the minuscule error. **Center:** The distance to filaments from galaxy clusters. Comparing the left panel to the center panel, we see that clearly clusters are closer to filaments than a randomly select galaxy. **Right:** The inverse of the cube root of number density  $\bar{n}(z)$ . This quantity has the unit of distance and is generally proportional to the average distance between galaxies. Distances to filaments from both galaxies and clusters have a similar trend as  $\bar{n}(z)^{-1/3}$ . This reveals that the increasing pattern in redshift is due to the change in number density.



Notation	Definition	Unit	Remark
$z_{\text{low}}$	Redshift value $t$		$z_{\text{low}} \leq z < z_{\text{low}} + 0.005$
$N$	Galaxy number		
$N_{\text{GC}}$	Galaxy cluster number		
$h_{deg}$	Smoothing bandwidth	degree	
$h_{\text{Mpc}}$	Smoothing bandwidth	Mpc	
$p_{\text{mean}}$	Mean galaxy density	degree <sup>-2</sup>	
$p_{\text{rms}}$	RMS of galaxy density	degree <sup>-2</sup>	
$F_{\text{density}}$	Mean galaxy density on filaments	degree <sup>-2</sup>	
$dF$	Mean galaxy distance to filaments	Mpc	
$dF_H$	Mean galaxy distance to high density filaments	Mpc	
$dF_{gc}$	Mean cluster distance to filaments	Mpc	-1: $N_{\text{GC}} = 0$
$dF_{gc,H}$	Mean cluster distance to high density filaments	Mpc	-1: $N_{\text{GC}} = 0$
$UM_{Q1}$	First quantile for uncertainty of filaments	Mpc	
$UM_{med}$	Median uncertainty of filaments	Mpc	
$UM_{avg}$	Mean uncertainty of filaments	Mpc	
$UM_{Q3}$	Third quantile for uncertainty of filaments	Mpc	
$UM_{rms}$	Uncertainty fluctuation (RMS) of filaments	Mpc	

**Table 2.** Definition of entries in the catalogue-description file.

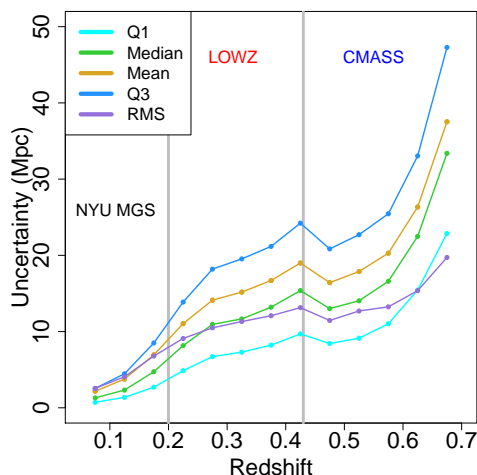


**Figure 8.** Summary statistics showing how filament uncertainty measures evolve with redshift. The increasing pattern along redshift for all uncertainty measures is from the change in number density (c.f. right panel of Figure 7).

Rozo & Rykoff 2014);  $dF_{gc,H}$  is similar to  $dF_H$  but is evaluated at each galaxy cluster. The quantity  $dF_{gc,H}$  is the mean distance to the high-density filament from galaxy clusters. If  $N_{\text{GC}} = 0$ , both  $dF_{gc}$  and  $dF_{gc,H}$  are set to be -1. The center panel of Figure 7 shows the mean distance of galaxy clusters  $dF_{gc}$  under various redshifts. Basically,  $dF_{gc}$  follows a similar trend as  $dF$  but has a lower value, indicating that, on average, clusters are closer to filaments than a randomly selected galaxy.

Finally, the five quantities  $UM_{Q1}$ ,  $UM_{med}$ ,  $UM_{avg}$ ,  $UM_{Q3}$  and  $UM_{RMS}$  are summary statistics for the uncertainty distributes on filaments within each slice. These quantities are the first quantile (25%), median, mean, third quantile (75%) and root mean square for all the uncertainty values on filament. The uncertainties are computed using the bootstrap method of Chen et al. (2015). The summary at different redshifts is presented in Figure 8. The increase of the un-

certainty as a function of redshift is due to the change in number density (c.f. right panel of Figure 7).

## 5.1 Filament Evolution

The metric we adopt for quantifying the evolution of filaments is the ratio of galaxies and clusters within filaments at different redshifts. To account for the difference in number density due to the redshift, we first derive a scaled distance to the nearest filament for each galaxy (and cluster) using the smoothing parameter and uncertainty measures. Let  $D$  be the distance to filament from a galaxy, and  $\pi$  be the nearest point on a filament and  $U$  be the uncertainty measure at  $\pi$  (the uncertainty measure is defined only for points on filaments). The scaled distance (to the nearest filaments) from a specified galaxy is defined as

$$S = \sqrt{\frac{D^2 + U^2}{h^2}}, \quad (3)$$

where  $h$  is the smoothing parameter. We divide the distance by smoothing parameter so that this scaled distance is comparable from slice to slice (otherwise for galaxies at lower redshift,  $S$  will be much smaller than galaxies at higher redshift). A galaxy (or a cluster) is classified as *within* a filament if

$$S \leq 0.3246. \quad (4)$$

The constant 0.3246 arises from the density of Gaussian distribution. Let  $\phi(x) = \frac{1}{\sqrt{2\pi}} e^{-x^2/2}$  be the Gaussian distribution. Then

$$\frac{\phi(0.3246)}{\phi(0)} \approx 0.9.$$

If we convolve a true filament with a Gaussian, the resulting filamentary regions are those points with potential above 90%. i.e., galaxies or clusters within these regions are recognized as being ‘within’ filaments.

Figure 9 displays the proportion of galaxies from different catalogues as well as clusters that are ‘within’ filaments using criterion (3) and (4). The three color bars (black, red and blue) are the ‘mean’ proportion for NYU MGS, LOWZ

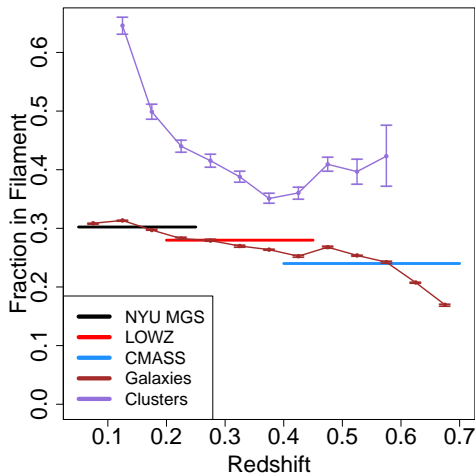


**Figure 9.** Fraction of galaxies and clusters within filaments at different redshifts. The fraction of clusters within filaments (purple curves) roughly follows the trend of number density at different redshifts. In general, our result suggests that roughly 30% galaxies are in filaments.

and CMASS galaxies. The brown line is the result for galaxies from all the samples at different redshifts, and purple lines are the ratios for clusters. For galaxies, there is a clear decrease with redshifts, with a small bump at  $z \sim 0.5$ . This region is the beginning of CMASS sample, so that the number density is in fact increasing (see Figure 5), therefore our detection power is increasing. The width of error bar at Figure 8 also drops at the  $z = 0.5$ , indicating the same pattern. This effect is stronger for galaxy clusters.

Another useful statistic is the proportion of ‘stable’ filament points. We classify a filament point as *stable* if

$$UM \leq \overline{UM} + kUM_{RMS}, \quad (5)$$

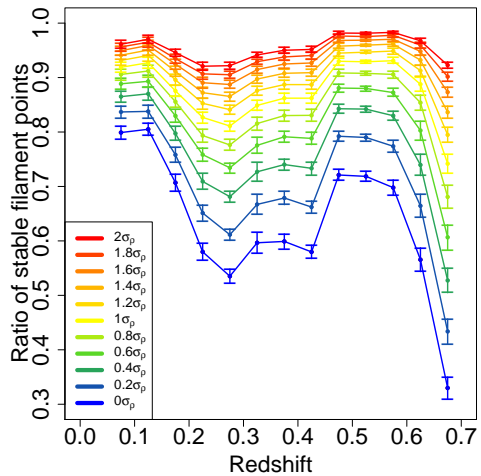
where  $\overline{UM}$  and  $UM_{RMS}$  are the mean and the root mean square of the uncertainty over all filament points across every slice. The number  $k$  is the threshold level for defining a filament point as stable.

Figure 10 displays the proportion of stable filaments as a function of redshift under  $k$  ranging from 0 to 2. For all  $k$ , we see a clear pattern that the ratio first drops and then increases and drops again. This phenomenon is even stronger at smaller  $k$ . This pattern is similar to that of the number of observations at each slice (cf. Figure 5).

## 5.2 Filament Intersections

As mentioned in the introduction, SCMS filaments have an attractive property that they have good agreement with known galaxy clusters. Chen et al. (2015) demonstrated that most clusters are generally close to the detected filaments. In this section, we identify intersections for filaments and compare them to locations of galaxy clusters.

To obtain filament intersections, we apply a simple algorithm derived from metric graph reconstruction (Aanjaneya et al. 2012; Lecci et al. 2013), a method from computational



**Figure 10.** Ratio of ‘stable’ filament points at different redshifts under different threshold levels. Changing the threshold for stability reveals an interesting pattern for the ratio of stable filament points, which is in a similar trend of number of galaxies within each slice. See Section 5.1 for further details.

geometry, to the filaments detected by SCMS<sup>3</sup>. The implementation details can be found in Appendix A.

Figure 2 presents an example of applying this detection algorithm to our filament maps. The orange color points are intersections. The detection algorithm clearly successfully identifies the intersection points, and most galaxy clusters are close to these points.

To quantify the closeness of clusters to intersection points, we compute the distance from galaxy clusters to the intersection points at different redshifts and compare this distance statistic to the distance from a random galaxy point to the intersection. Figure 11 shows the distribution of distances from clusters (red) versus distance from galaxies. We use the one-sided KS-test to compare the difference in distribution; the result is given in Table 3. The clusters are significantly closer to intersections for filaments compared to galaxies. The worst case (largest p-value) is at  $0.4 < z < 0.45$ . This region corresponds to the boundary between LOWZ and CMASS samples and is the region with the smallest number density of galaxies (cf. Figure 5). Thus, our filament detection algorithm lacks statistical power at this region, so it is expected that the p-value is largest here.

## 6 MAGNITUDE AND DISTANCE TO FILAMENTS

We use the filament maps to investigate the relation between a galaxy’s magnitude and its distance to filaments. Specifically, we wish to determine whether galaxies near filaments tend to be more luminous.

We separately analyze each of the three galaxy catalogues (NYU MGS, LOWZ and CMASS). For each catalogue, we slice the redshift into several bins with width  $\Delta z = 0.005$  that matches our filament maps. We focus on

<sup>3</sup> We also provide the intersections of filaments in <https://sites.google.com/site/yenchic/catalogue>.

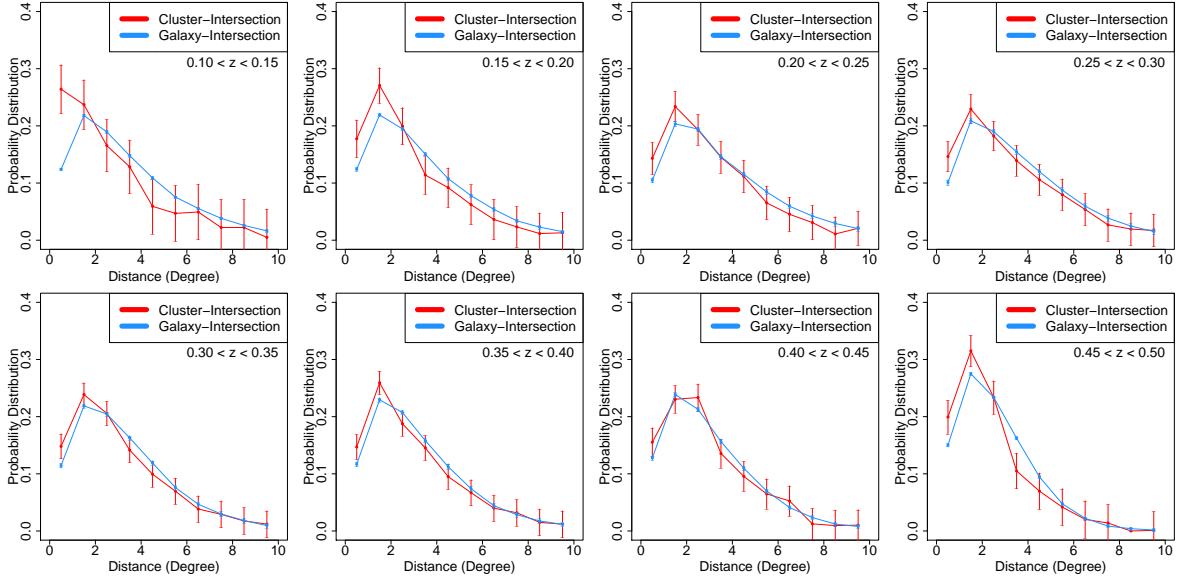


**Figure 11.** Distributions of distances from clusters (red) and galaxies (blue) to intersection points. Each panel is the result for a particular redshift region. In every panel, we observe that clusters generally have shorter distances to intersection points than randomly selected galaxies. To make this statement quantitatively, we perform KS test for each pair of distributions. The result is given in Table 3.

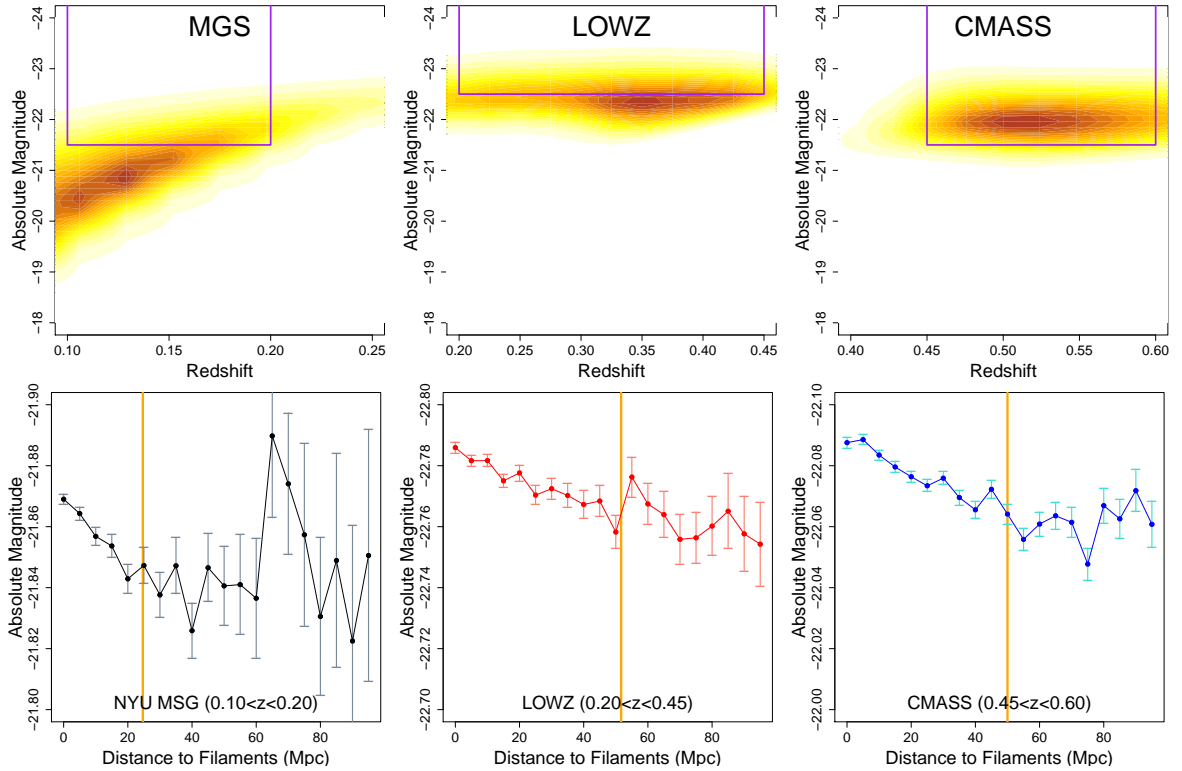


**Figure 12. Top row:** Selected magnitude regions for each sample (purple rectangles). Galaxies are selected within the purple rectangles to obtain a volume-limited sample. There is a strong cut on magnitude along the redshifts due to the observational limit. We have reversed the direction for Y-axis (magnitude) so that a galaxy in the upper region indicates that it is bright. **Bottom row:** Absolute magnitude ( $r$ -band) versus distance to filaments for volume-limited samples. The orange line is the boundary between decreasing pattern and random fluctuation. A piecewise linear regression is fitted to the data to select the orange line (selected values: 24.67 Mpc for NYU MGS, 51.67 Mpc for LOWZ and 57.34 Mpc for CMASS). On the left side of the orange line, there is a strong decreasing trend, while on the right side, the patterns exhibit random fluctuations.

Redshift	$p$ -value	Redshift	$p$ -value
0.100-0.150	$2.79 \times 10^{-11}$	0.300-0.350	$2.68 \times 10^{-6}$
0.150-0.200	$2.55 \times 10^{-9}$	0.350-0.400	$2.16 \times 10^{-7}$
0.200-0.250	$2.58 \times 10^{-8}$	0.400-0.450	$1.28 \times 10^{-2}$
0.250-0.300	$4.47 \times 10^{-8}$	0.450-0.500	$4.95 \times 10^{-8}$

**Table 3.** Significances generated from a one-sided, two-sample KS test, for the null hypothesis that galaxy clusters lie at the same average distance from intersections as field galaxies.  $p$ -value is a statistical quantity to measure the significance. Typically, the usual rejection rule requires  $p < 0.05$ .

the regions  $0.1 < z < 0.6$  since the reMaPPer cluster catalogue mainly covers this redshift range. For each slice, we remove galaxies whose distance to galaxy clusters is less than 5 Mpc, thus eliminating the effect of galaxy clusters.

Since the SDSS dataset is not volume limited, we had to apply additional constraints to construct a volume-limited sample. Our selection rule is

$$\begin{aligned}
 (\text{NYU MGS}) \quad M_r &< -21.5, & 0.10 \leq z \leq 0.20 \\
 (\text{LOWZ}) \quad M_r &< -22.5, & 0.20 \leq z \leq 0.45 \\
 (\text{CMASS}) \quad M_r &< -21.5, & 0.45 \leq z \leq 0.60.
 \end{aligned}$$

The first row of Figure 12 shows the luminosity-redshift region within each of the NYU MGS, LOWZ and CMASS samples. This figure reveals the strong luminosity-redshift dependence.

The bottom row of Figure 12 presents the relation between magnitude and distance to filaments for each sample. Every sample processes a strong dependence of magnitude and distance (to filaments). Galaxies near filaments are generally more luminous than those at greater distance from filaments. This relation vanishes after certain range of distance (distance to the nearest filament). To determine where the increasing pattern disappears, we fit the following piecewise linear function:

$$M(x) = \begin{cases} \beta_0 + \beta_1 x & \text{if } x < x_c \\ \beta_0 + \beta_1 x_c & \text{if } x \geq x_c \end{cases} \quad (6)$$

where  $M(x)$  is the magnitude and  $x$  is the distance to filaments. Namely,  $M(x)$  is a linear curve when  $x$  is less than the critical distance  $x_c$  and is a constant after the critical distance. The optimal fit suggests that  $x_c$  for NYU MGS sample is 24.67 Mpc, for LOWZ sample is 51.67 Mpc and for CMASS sample is 57.34 Mpc. This phenomena can be explained by the uncertainty of filaments. The uncertainty in filaments will smooth out the impact that the distance to filaments has on magnitude. From Figure 8, the uncertainties for filaments within the NYU MGS, LOWZ and CMASS samples are 8, 15, 20 Mpc, respectively. This is why the effect spans longer distances at high redshifts.

The slope  $\beta_1$  in (6) determines the strength, as well as the significance, for the decreasing pattern and is given in Table 4. According to Table 4, we observe a significant evidence (at  $6.1\sigma - 12.3\sigma$ ) that the luminosity is indeed negatively correlated with the distance before the critical distance.

## 7 CONCLUSION

In this paper, we construct a series of two-dimensional filament maps from SDSS data using the SCMS algorithm. We provide several statistics to measure the properties of the filamentary maps we constructed at each redshift. These measurements may be used to study the evolution of the Universe and constrain cosmology.

We compare our publicly available catalogue to the existing catalogues for filaments introduced in Sousbie et al. (2008), Jasche et al. (2010), Smith et al. (2012), and Tempel et al. (2014). Each of these catalogues provide some analysis for the large-scale structure over the whole Universe by using different models for filaments. However, none of them is publicly available. This makes it difficult for other research groups to use these catalogues to analyze filaments. Moreover, unlike our catalogue all these catalogues do not provide any measurement on the errors for filament detection and only focus on the small redshift range (less than  $z = 0.25$ ). To our knowledge, our filament catalogue is by far the only filament catalogue for redshift  $z > 0.25$  in the SDSS.

We apply our filament maps to investigate the galaxy luminosity-filament distance relation using a volume-limited sample. There is a long distance effect from filaments (more than 20 Mpc) on the brightness of galaxies, which is at a different scale than Guo et al. (2015), where they found a similar pattern at a much smaller scale (distances less than 0.71 Mpc). Although part of the long distance effect can be explained by the errors of filaments, our results suggest that the correlation between galaxy magnitude and distance to filaments may extend over distances  $\gg 1$  Mpc.

## ACKNOWLEDGMENTS

We thank Hung-Jin Huang, Rachel Mandelbaum, Michael Strauss, and Hy Trac for useful discussions and comments. This work is supported in part by the Department of Energy under grant DESC0011114; YC is supported by William S. Dietrich II Presidential Ph.D. Fellowship; SH is supported in part by DOE-ASC, NASA and NSF; CG is supported in part by DOE and NSF; LW is supported by NSF. Funding for SDSS-III has been provided by the Alfred P. Sloan Foundation, the Participating Institutions, the National Science Foundation, and the U.S. Department of Energy Office of Science. The SDSS-III web site is <http://www.sdss3.org/>.

SDSS-III is managed by the Astrophysical Research Consortium for the Participating Institutions of the SDSS-III Collaboration including the University of Arizona, the Brazilian Participation Group, Brookhaven National Laboratory, Carnegie Mellon University, University of Florida, the French Participation Group, the German Participation Group, Harvard University, the Instituto de Astrofísica de Canarias, the Michigan State/Notre Dame/JINA Participation Group, Johns Hopkins University, Lawrence Berkeley National Laboratory, Max Planck Institute for Astrophysics, Max Planck Institute for Extraterrestrial Physics, New Mexico State University, New York University, Ohio State University, Pennsylvania State University, University of Portsmouth, Princeton University, the Spanish Participation Group, University of Tokyo, University of Utah,

		NYU MGS ( $z = 0.10 - 0.20$ )	LOWZ ( $z = 0.20 - 0.43$ )	CMASS ( $z = 0.43 - 0.70$ )
Slope <sup>†</sup>	Estimate	$-11.82 \times 10^{-04}$	$-4.34 \times 10^{-04}$	$-5.13 \times 10^{-04}$
	Standard Error	$1.92 \times 10^{-04}$	$6.53 \times 10^{-05}$	$4.17 \times 10^{-05}$
	Significance	$6.15\sigma$	$6.64\sigma$	$12.31\sigma$

**Table 4.** Linear fit for the three catalogues for absolute magnitude versus distance to filaments. † A negative slope indicates that the luminosity decreases as the distance (to filaments) increases.

Vanderbilt University, University of Virginia, University of Washington, and Yale University.

## APPENDIX A: ALGORITHM FOR DETECTING INTERSECTION POINTS

In this section, we describe the metric graph reconstruction algorithm (Aanjaneya et al. 2012; Lecci et al. 2013) for detecting intersection points of filaments. Our algorithm examines every point on the filaments and assigns it into the ‘intersection’ class or ‘non-intersection’ class using the following process. Let  $x$  be a point we wish to examine.

1. Keep those data points whose distance to  $x$  is between  $r_{in}$  and  $r_{out}$ , two parameters.
2. Cluster the remaining points using hierarchical clustering with radius  $r_{sep}$ , i.e., partitioning points into several groups such that group-group distance is greater than  $r_{sep}$ .
3. Count the number of groups from previous step. If the number of groups is greater or equal to three, classify  $x$  as an *intersection* point, otherwise classify it as *non-intersection*.

The idea behind this algorithm is that when a point is at the intersection, other points around this point within the shell (form by  $r_{in}$  and  $r_{out}$ ) should have at least three clusters. For an edge point, there will be two clusters and for the end point, there is only one cluster. Points near the same intersection may all be classified as intersection points; we use the mean location as intersection point:

$$r_{in} = 2h/3, \quad r_{out} = 2r_{in}, \quad r_{sep} = (r_{in} + r_{out})/2. \quad (A1)$$

This choice of parameters is ad hoc but works well in practice.

## REFERENCES

- Aanjaneya M., Chazal F., Chen D., Glisse M., Guibas L., Morozov D., 2012, *International Journal of Computational Geometry and Applications*, 22, 305
- Abazajian K. N., et al., 2009, *ApJS*, 182, 543
- Abell G. O., Corwin Jr. H. G., Olowin R. P., 1989, *ApJS*, 70, 1
- Adelman-McCarthy J. K., et al., 2008, *ApJS*, 175, 297
- Aihara H., et al., 2011, *ApJS*, 193, 29
- Alam S., et al., 2015, *ApJS*, 219, 12
- Anderson L., et al., 2012, *MNRAS*, 427, 3435
- Anderson L., et al., 2014, *MNRAS*, 439, 83
- Aragón-Calvo M. A., Jones B. J. T., van de Weygaert R., van der Hulst J. M., 2007, *A&A*, 474, 315
- Aragón-Calvo M. A., van de Weygaert R., Jones B. J. T., 2010a, *MNRAS*, 408, 2163
- Aragón-Calvo M. A., Platen E., van de Weygaert R., Szalay A. S., 2010b, *ApJ*, 723, 364
- Blanton M. R., Lin H., Lupton R. H., Maley F. M., Young N., Zehavi I., Loveday J., 2003, *AJ*, 125, 2276
- Blanton M. R., et al., 2005, *AJ*, 129, 2562
- Bolton A. S., et al., 2012, *AJ*, 144, 144
- Bond J. R., Kofman L., Pogosyan D., 1996, *Nature*, 380, 603
- Bond N. A., Strauss M. A., Cen R., 2010a, *MNRAS*, 406, 1609
- Bond N. A., Strauss M. A., Cen R., 2010b, *MNRAS*, 409, 156
- Chen Y.-C., Genovese C. R., Wasserman L., 2014a, preprint, ([arXiv:1406.5663](https://arxiv.org/abs/1406.5663))
- Chen Y.-C., Genovese C. R., Wasserman L., 2014b, preprint, ([arXiv:1406.1803](https://arxiv.org/abs/1406.1803))
- Chen Y.-C., Ho S., Freeman P. E., Genovese C. R., Wasserman L., 2015, preprint, ([arXiv:1501.05303](https://arxiv.org/abs/1501.05303))
- Codis S., et al., 2015, *MNRAS*, 448, 3391
- Colberg J. M., Krughoff K. S., Connolly A. J., 2005, *MNRAS*, 359, 272
- Dawson K. S., et al., 2013, *AJ*, 145, 10
- Doi M., et al., 2010, *AJ*, 139, 1628
- Dolag K., Meneghetti M., Moscardini L., Rasia E., Bonaldi A., 2006, *MNRAS*, 370, 656
- Eberly D., 1996, *Ridges in Image and Data Analysis*. Springer
- Efron B., 1979, *Annals of Statistics*, 7, 1
- Eisenstein D. J., et al., 2001, *AJ*, 122, 2267
- Eisenstein D. J., et al., 2011, *AJ*, 142, 72
- Forero-Romero J. E., Contreras S., Padilla N., 2014, *MNRAS*, 443, 1090
- Fukugita M., Ichikawa T., Gunn J. E., Doi M., Shimasaku K., Schneider D. P., 1996, *AJ*, 111, 1748
- Genovese C. R., Perone-Pacífico M., Verdinelli I., Wasserman L., 2014, *The Annals of Statistics*, 42, 1511
- Gunn J. E., et al., 1998, *AJ*, 116, 3040
- Gunn J. E., et al., 2006, *AJ*, 131, 2332
- Guo Q., Tempel E., Libeskind N. I., 2015, *ApJ*, 800, 112
- Hahn O., Porciani C., Carollo C. M., Dekel A., 2007a, *MNRAS*, 375, 489
- Hahn O., Carollo C. M., Porciani C., Dekel A., 2007b, *MNRAS*, 381, 41
- Hahn O., Porciani C., Dekel A., Carollo C. M., 2009, *MNRAS*, 398, 1742
- Jasche J., Kitaura F. S., Li C., Enßlin T. A., 2010, *MNRAS*, 409, 355
- Jenkins A., et al., 1998, *ApJ*, 499, 20
- Jones B. J. T., van de Weygaert R., Aragón-Calvo M. A., 2010, *MNRAS*, 408, 897
- Lecci F., Rinaldo A., Wasserman L., 2013, preprint, ([arXiv:1305.1212](https://arxiv.org/abs/1305.1212))

- Lupton R., Gunn J. E., Ivezić Z., Knapp G. R., Kent S., 2001, in Harnden Jr. F. R., Primi F. A., Payne H. E., eds, *Astronomical Society of the Pacific Conference Series Vol. 238, Astronomical Data Analysis Software and Systems X*. p. 269 ([arXiv:astro-ph/0101420](#))
- Mantz A., Allen S. W., Ebeling H., Rapetti D., Drlica-Wagner A., 2010, *MNRAS*, **406**, 1773
- Maraston C., et al., 2013, *MNRAS*, **435**, 2764
- Menanteau F., et al., 2013, *ApJ*, **765**, 67
- Novikov D., Colombi S., Doré O., 2006, *MNRAS*, **366**, 1201
- Ozertem U., Erdogmus D., 2011, *JMLR*, **12**, 1249
- Padmanabhan N., et al., 2008, *ApJ*, **674**, 1217
- Paz D. J., Staszczyn F., Padilla N. D., 2008, *MNRAS*, **389**, 1127
- Pier J. R., Munn J. A., Hindsley R. B., Hennessy G. S., Kent S. M., Lupton R. H., Ivezić Ž., 2003, *AJ*, **125**, 1559
- Piffaretti R., Arnaud M., Pratt G. W., Pointecouteau E., Melin J.-B., 2011, *A&A*, **534**, A109
- Planck Collaboration et al., 2011, *A&A*, **536**, A8
- Rozo E., Rykoff E. S., 2014, *ApJ*, **783**, 80
- Rykoff E. S., et al., 2014, *ApJ*, **785**, 104
- Smee S. A., et al., 2013, *AJ*, **146**, 32
- Smith A. G., Hopkins A. M., Hunstead R. W., Pimblett K. A., 2012, *MNRAS*, **422**, 25
- Sousbie T., 2011, *MNRAS*, **414**, 350
- Sousbie T., Pichon C., Courtois H., Colombi S., Novikov D., 2008, *ApJ*, **672**, L1
- Springel V., et al., 2005, *Nature*, **435**, 629
- Strauss M. A., et al., 2002, *AJ*, **124**, 1810
- Tempel E., Stoica R. S., Martínez V. J., Liivamägi L. J., Castellan G., Saar E., 2014, *MNRAS*, **438**, 3465
- Wasserman L., 2006, *All of nonparametric statistics*. Springer Science & Business Media
- York D. G., et al., 2000, *AJ*, **120**, 1579
- Zhang Y., Yang X., Faltenbacher A., Springel V., Lin W., Wang H., 2009, *ApJ*, **706**, 747
- Zhang Y., Yang X., Wang H., Wang L., Mo H. J., van den Bosch F. C., 2013, *ApJ*, **779**, 160

This paper has been typeset from a  $\text{T}_{\text{E}}\text{X}/\text{L}^{\text{A}}\text{T}_{\text{E}}\text{X}$  file prepared by the author.